Title.
Spectral X-ray phase contrast imaging with a CdTe photon-counting detector

Author name and affiliations.
Carlos Navarrete[a], Simon Procz[b], Michael Kilian Schütz[b], Gerardo Roque[a], Julian Fey[b], Carlos Avila[a], Alessandro Olivo[c] and Michael Fiederle[b]

[a] Universidad de Los Andes, Departamento de Física, Cra 1 Nº 18A – 12, 111711, Bogotá, Colombia
[b] Freiburg Materials Research Center (FMF), Stefan-Meier-Str. 21, 79104 Freiburg, Germany
[c] Department of Medical Physics and Biomedical engineering, University College London, Malet Place, Gower Street, WC1E 6BT London, United Kingdom

Corresponding author.
Carlos Navarrete
Phone: +57 321-3439998
Mail: cf.navarrete969@uniandes.edu.co
Postal address: Universidad de Los Andes, Departamento de Física, Cra 1 Nº 18A – 12, 111711, Bogotá, Colombia

Abstract.
The present study focuses on the implementation of two X-ray phase contrast imaging (XPCI) techniques: free-space propagation (FSP) and single mask edge illumination (SM-EI) with a microfocus polychromatic X-ray source and a Timepix3 photon-counting detector with a CdTe sensor. This detector offers high spatial resolution, high detection efficiency and it is able to simultaneously record information about Time-over-Threshold (ToT) and Time-of-Arrival (ToA) for each X-ray photon. All these features play a key role in enabling an improvement of XPCI image quality, especially through spectral analysis, since it is possible to measure the energy of each incident X-ray photon. Measurements of phase contrast and contrast-to-noise ratio (CNR) are presented for different energy bins within the typical spectrum of soft X-ray imaging. It is shown that a significant enhancement of XPCI image quality can be obtained, for both implemented techniques, by performing pixel clustering to correct for charge sharing and by introducing some degree of energy-weighting.

Keywords.
X-ray imaging; Phase-contrast; Photon-counting detector; Timepix; Image quality.

1.   Introduction

1.1.   X-ray Phase Contrast Imaging

X-ray Phase Contrast Imaging (XPCI) is a well-established tool for the nondestructive examination of diverse types of samples. It relies on the phase shift suffered by X-rays when traversing a sample, which is driven by the unit decrement of the real part of the complex refractive index δ. Conversely, attenuation properties are related to the imaginary term β. Depending on the incident X-ray spectrum and the material being examined, δ can be up to three orders of magnitude greater than β, consequently, XPCI techniques allow the visualization of low contrast details previously invisible to conventional absorption methods [1].

XPCI can be exploited for several applications, including biomedical imaging [2-5], material science [6, 7], security [8] and industrial quality inspection [9, 10]. For such purposes, different methods have been developed to record the phase shift. Among them, Free-space Propagation and Single Mask Edge Illumination (SM-EI) XPCI are two approaches suitable for laboratory implementation.

1.1.1.   Free-space Propagation (FSP) XPCI

Free-space propagation XPCI was introduced by Snigirev *et al.* [11] with monochromatic synchrotron radiation. They demonstrated that image effects due to phase shifts can be observed with a source of sufficient spatial coherence and by increasing the distance between the sample and the detector. As shown in Fig. 1a, after being shifted, the wavefronts propagate until they form an interference pattern, which in the near field can be seen as an edge enhancement. The principle was extended to polychromatic laboratory sources by Wilkins *et al.* [12] and later its potential for imaging low attenuation samples was demonstrated [13, 14]. FSP XPCI has been extensively implemented with both synchrotron [15, 16] and polychromatic [17, 18] radiation; however, due to its high lateral spatial coherence requirements, X-ray laboratory sources with a very small focal spot (on the order of 10 µm) are required.

Since both absorption and phase signals contribute to the image formation in FSP XPCI, the quantitative phase-retrieval problem has been extensively studied. Until now, homogeneity assumptions or *a priori* information on the sample are required for single image phase-retrieval [19-21]. Therefore, multiple images acquired at different propagation distances are necessary to obtain a quantitative separation of phase and attenuation [22].
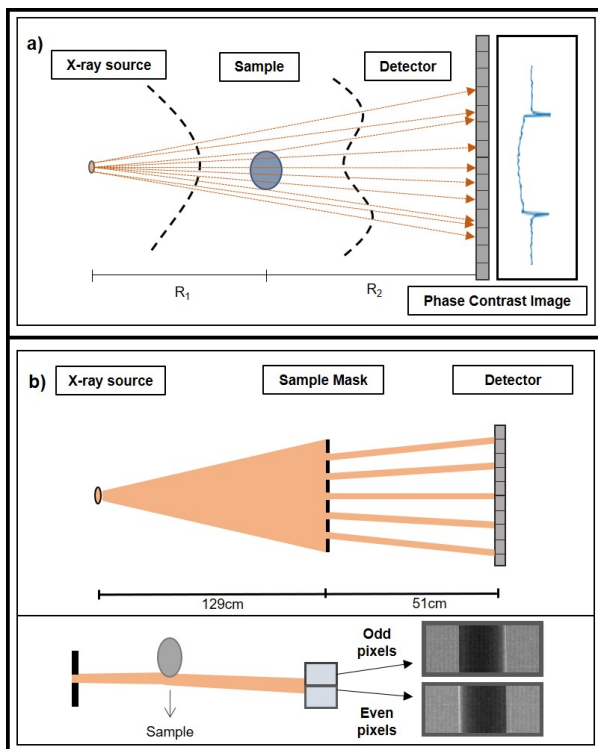
Fig. 1. a) Schematic set up of free-space propagation XPCI. The incoming wave front is perturbed by the sample and an interference pattern is created at the detector, which is placed at a distance R_2. b) Schematic set up of single mask edge illumination XPCI. The mask apertures create beamlets which are aligned with the pixel edge s. Odd and even pixels can be separated to obtain two images with inversed phase signals, as shown in the bottom panel.

1.1.2. Single Mask Edge Illumination (SM-EI) XPCI

SM-EI is based on the Edge-Illumination principle, originally described by Olivo *et al.* [23]. In the original set-up, two periodic masks are used: the sample mask, placed before the sample, and the detector mask, located in front of the detector. The sample mask reshapes the incoming beam into smaller beamlets that hit the apertures of the detector mask to create the Edge-Illumination condition, in which only a fraction of the beamlets impinges on the pixel active surface. The detector mask also serves to reduce the smoothing of the phase signal caused by non-ideal pixel Point Spread Functions (PSF) [24]. However, with recent photon-counting devices with a more defined PSF, such as those from the Medipix and Timepix families, the detector mask can be removed and the beamlets aligned with the boundary between two pixels columns (or rows, depending on the mask orientation). This allows for the detection of beam displacement after it traverses the sample, as shown in Fig. 1b [25].

By separating the odd and even pixel columns (or rows), this set-up allows for phase and attenuation signal separation with a single acquisition, since it gives two images with equivalent absorption information but opposite differential phase contrast signals. So long as the PSF is sufficiently sharp [26], the single mask arrangement can provide comparable phase sensitivity to the double-mask configuration, with a tradeoff between resolution and image: the spatial resolution is halved, and the image statistics is doubled. Besides, with a mask design like the one proposed by Krejci *et al.* [27], in which the beamlets are shaped so they hit the region between four pixels instead of two, the system can be extended to provide 2D sensitivity, even in CT [28].

1.1.3. XPCI with spectral photon-counting detectors

The development of photon-counting detectors with energy-resolving capabilities has motivated the study of spectral X-ray imaging for different applications. Recently, it was combined with XPCI to improve the image quality of various phase-sensitive methods. The Medipix detector was used by Das *et al.* [29, 30], to separate the photons into multiple energy bins, which allows for single-shot phase and absorption retrieval. The approach was developed with both the Free-space propagation and the Double Mask Edge Illumination techniques. Later, the same concept was derived and applied to simulated data by Wang *et al.* with the Grating Interferometric method [31].

An additional advantage of spectral photon-counting devices is the possibility of image quality improvements obtained by employing energy weighting factors. The concept of energy-weighting was first introduced for conventional X-ray imaging by Giersch *et al.* with a Medipix2 detector [32, 33], by showing that it can be used to significantly improve image quality. In XPCI, the concept was used for the Grating Interferometric technique, motivated by the fact that interferometers are designed for specific energy [34]. In contrast, SM-EI XPCI was demonstrated to be fully achromatic by Endrizzi *et al.* [35]. This lack of increased weighting of specific spectral channels, shared with FSP XPCI, means that a statistical approach to weighting factors can be implemented to increase image quality.

1.2. The Timepix3 detector

The Timepix3 is a hybrid pixel photon-counting detector, fabricated in a CMOS 130 nm process. The detector has 256x256 pixels with a pixel pitch of 55 μm. It allows the acquisition of time and energy information for each incident photon by simultaneously measuring the time-of-arrival (ToA) and time-over-threshold (ToT) of each X-ray photon [36]. The electronics of the Timepix3 chip can be bump bonded to diverse sensor materials such as Si, CdTe, CdZnTe, Ge, or GaAs. In particular, its high atomic number, high density, wide energy bandgap and high resistivity, make the CdTe semiconductor suitable for room temperature operation with high detection efficiency for X-rays [37]. The energy-resolving properties of the detector, along with the good spatial resolution and high detection efficiency (when used with CdTe), have been exploited for several applications including medical imaging [38, 39], space sciences [40] and gamma camera imaging [41].

In this work, the time and energy information of the Timepix3 detector are used to study phase contrast and Contrast-to-Noise Ratio (CNR) in the FSP and SM-EI XPCI methods. The relevance of pixel clustering methods to correct for charge sharing effects (see section 2.4) is presented, and energy-weighting methods are implemented to increase image quality.

2. Materials and Methods

2.1. The experimental set-up

50 The FSP XPCI set-up consists of a Hamamatsu L10321 X-ray source (W-anode, 500 μm thick beryllium output window
51 and a nominal focal spot FWHM of 5 μm), a 1 mm thick CdTe-Timepix3 detector and a set of high-precision stepper
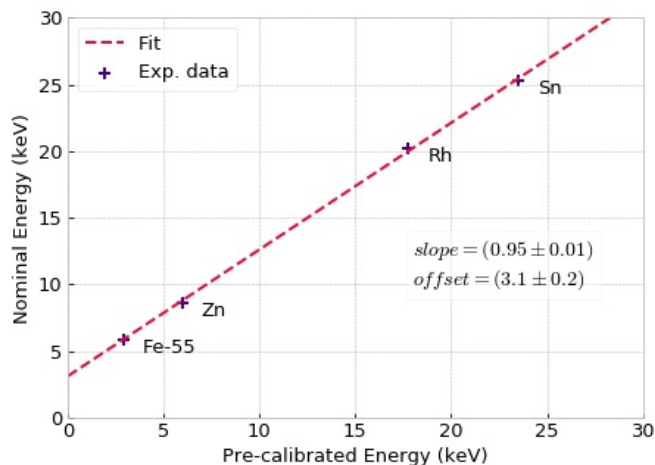52 motors with an accuracy of 1 μm, to position the sample.
53 For the SM-EI XPCI configuration, a sample mask with a period of 79 μm and an aperture size of 10 μm is also included.
54 The mask consists of a patterned gold layer with a nominal thickness of 100 μm, electroplated on a 500 μm thick
55 graphite substrate. In order to create the Edge Illumination condition for every other pixel column, an additional set of
56 high precision stepper motors (accuracy of 0.2 μm and 0.001 degrees for translation across and rotation around the
57 beam axis, respectively) is required to match the projected mask to twice the detector period (110 μm). Since the
58 sample mask absorbs part of the incoming beam, the sample is scanned laterally so as to expose all its parts to
59 radiation (sample "dithering"). Frames were acquired at eight dithering steps, i.e. eight different sample positions
60 spaced by approximately 10 μm. Since only a small fraction of the pixel and an even smaller fraction of the sample is
61 illuminated at each frame, due to the small aperture of the mask and the line-skipping nature of the SM-EI XPCI working
62 principle, this leads to a recombined image with 4x more resolution compared to the FSP XPCI case [42].

63
64 *2.2.   Verification of Timepix3 energy calibration*
65
66 The Timepix3 detector was manufactured and calibrated by Advacam, as described in [43]. To verify the calibration,
67 the global energy response of the detector was checked through X-ray fluorescence and radioactivity measurements.
68 The X-ray fluorescence peaks of Zn, Rh and Sn were measured, along with the radioactivity spectrum of Fe-55 for low
69 energies. Only single-pixel clusters were used for the calibration to avoid charge sharing effects.
70 The result of the energy calibration verification is shown in Fig. 2. The curve shows high linearity, with a slope of 0.95
71 and an offset of 3.1 keV between the nominal and measured peak energies. All measurements have been corrected
72 by this offset.
73

The figure shows a plot with axis labels "Nominal Energy (keV)" on the y-axis and "Pre-calibrated Energy (keV)" on the x-axis. Data points labeled Fe-55, Zn, Rh, Sn with a fit line. Text in figure: $slope = (0.95 \pm 0.01)$, $offset = (3.1 \pm 0.2)$.

74
75 Fig. 2. Linear fit of nominal vs pre-calibrated energy position. X-ray fluorescence and radioactive (Fe-55) spectrums
76 were measured for the verification.
77
78 2.3.   *Measurements*
79
80 Images were acquired at both 30 kVp and 50 kVp for FSP XPCI, and at 30 kVp only for SM-EI XPCI, to verify the
81 relevance of the method over different XPCI techniques. The tube current was operated below 30 μA in all cases to
82 avoid charge pile-up or pixel front-end saturation. The resulting milliampere-second values were 9.4 mAs and 3 mAs
83 for FSP XPCI at 30 kVp and 50 kVp, respectively. For SM-EI XPCI at 30 kVp, this value was 1.2 mAs for each of the
84 eight dithering steps, i.e., 9.4 mAs in total. The sample used was a nylon fiber with a diameter of 900 μm. The clustering
85 and energy bin analysis discussed in the following sections was carried out in full on the FSP XPCI measurements at
86 30 kVp, and some of it was repeated on the FSP XPCI at 50 kVp and SM-EI XPCI at 30 kVp measurements to prove
87 the generality of the presented approach.
88 The source-to-detector distance was 1.8 m for both XPCI methods. The magnification (M) for the FSP-XPCI was set
89 at 5x to avoid blurring caused by the focal spot. Conversely, for the SM-EI XPCI method, the fiber was placed very
90 close to the sample mask at a magnification of 1.3x. All images were flat-field corrected to account for detector
91 imperfections and beam non-uniformities.
92

2.4.   Pixel clustering methods

Charge sharing is a common effect in pixelated detectors such as Timepix3. This is caused by the spread of the charge carriers, generated by a single high-energy event, across multiple pixels. The spread is caused by diffusion and electrostatic repulsion between the charges generated in the semiconductor crystal. The charge is shared between adjacent pixels generating signals in more than one pixel, for a single incoming photon. Such a phenomenon reduces both the spatial and energy resolution of the detector. Previous studies have demonstrated that it increases with smaller pixel pitch, thicker sensor material, and lower bias voltage [44].

Since the Timepix3 detector allows for energy and time-of-arrival information of each event, charge sharing can be accounted for by forming clusters of events that initially belonged to a single high-energy photon. Such clusters are created by considering events that are close both in space and time-of-arrival. The total energy of the original event is then reconstructed by adding together the energy of the cluster and the count is allocated to the pixel closer to the cluster centroid. Some imprecisions are expected since part of the charge could go undetected if it does not exceed the counting threshold for some of the involved pixels.

In this work, the unclustered and clustered cases are compared. Note that an unclustered image is, in practice, the image that would be acquired by any small-pixel photon-counting detector without energy and time information.

2.5.   Energy bins analysis and energy weighting

The energy information was grouped in 3-keV energy bin images, i.e., for the 30-kVp acquisition, these bins were: 4-7 keV, 7-10 keV, 10-13 keV, 13-16 keV, 16-19 keV, 19-22 keV, 22-25 keV, 25-28 keV and 28-31 keV. This was done to study the energy dependence of phase contrast and contrast-to-noise ratio, and the effect of pixel clustering on different parts of the spectrum. XPCI techniques usually generate a pair of bright and dark fringes along the sample edges, and thus the contrast and CNR are calculated as follows:

$$Contrast = \frac{I_{max} - I_{min}}{I_{background}} \quad (1)$$

$$CNR = \frac{I_{max} - I_{min}}{\sigma(I_{background})} \quad (2)$$

where I_{max} and I_{min} are the maximum and minimum signals across the nylon fiber profile, respectively, and $\sigma(I_{background})$ is the standard deviation of the image in the background region.

With non-spectroscopic photon-counting detectors, the energy bins are weighted by the X-ray source spectrum. However, when spectroscopic information is incorporated and images at different energy bins are extracted, the weights can be modified to maximise the CNR in the image. In this work, the energy weighting formulation derived by Schmidt [45] was employed, although while using the contrast in each energy bin as the weighting factor:

$$w_n = \frac{C_n}{\sum_i C_i} \quad (3)$$

Later, the images are recombined to give a final image which is referred to as 'energy-weighted image':

$$I_{combined} = \sum_i w_i I_i \quad (4)$$

While Schmidt introduced energy weighting for conventional attenuation-based X-ray imaging it is shown here that the same approach leads to higher image quality also for the FSP and SM-EI XPCI methods. The energy-weighted image is compared with the 'unclustered image' and the 'clustered image'. The former is the case where neither clustering nor energy-weighting are applied, while only clustering (but no energy-weighting) is applied to the latter.

3.   Results

3.1.   Energy spectrum

Full spectra at both 30 and 50 kVp were acquired using the Timepix3 spectral capability, and the unclustered and clustered cases were compared (see Fig. 3). The unclustered spectra show a significantly stronger low-energy peak which is caused by charge sharing events. Such counts correspond to approximately 40% and 50% for the 30 kVp and 50 kVp cases, respectively. The clustered spectra show that clustering methods are key to reconstruct high-energy events (above 15 keV), and that without them, limited spectroscopic information can be retrieved above 25 keV. As presented in the following sections, this spectrum correction is relevant to exploit the information carried by all photons for both XPCI methods, which leads to higher phase contrast.
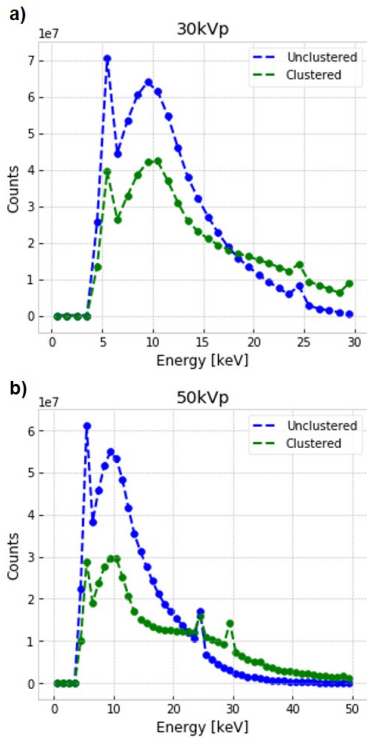
Fig. 3. Histograms of experimental spectra for unclustered and clustered cases for 30 kVp (top) and 50 kVp (bottom).

3.2.   Clustering and spectral analysis

In Fig. 4, the images obtained at each energy bin are presented, and the unclustered (Fig. 4a) and clustered (Fig. 4b) cases are compared. In both cases, the energy dependence of the attenuation and phase signals is clearly noticeable. Due to the low attenuation and phase coefficients of the nylon fiber, contrast is stronger in the low-energy bins. However, it should be noted that, despite the negligible absorption of the fibers at the highest energies, the phase signal still permits to distinguish the fiber shape. This is significantly improved by the reconstruction of events with the clustering method, which reduces the noise substantially in the three highest energy bins.
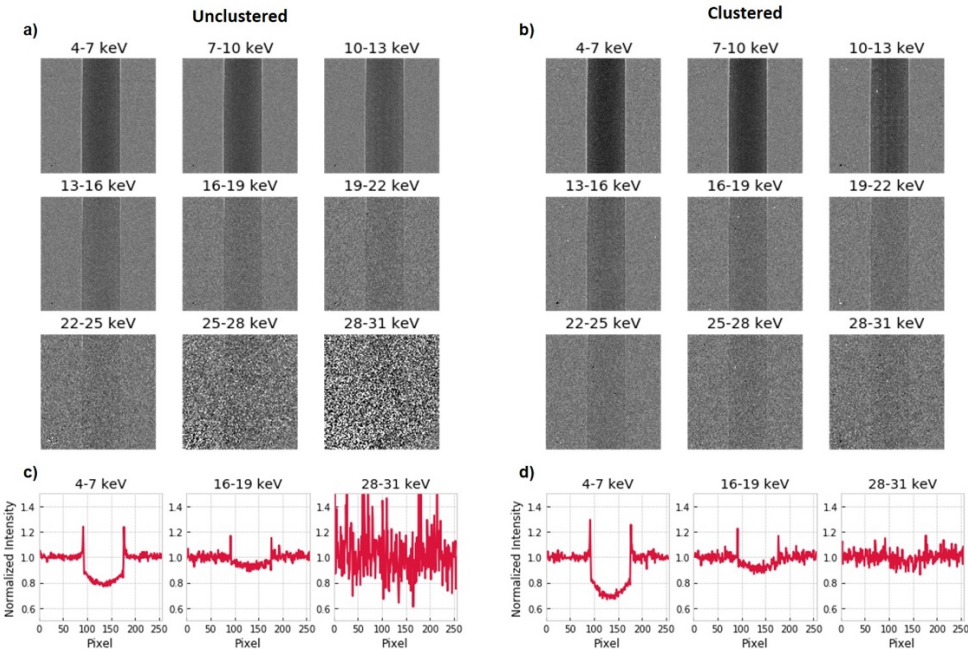

Fig. 4. Images retrieved for each 3-keV energy bin at 30 kVp a) without clustering and b) with clustering. The averaged horizontal profile along five rows is also shown for 3 different energy bins: 4-7 keV, 16-19 keV and 28-31 keV; c) without clustering and d) with clustering.

6

The effect of pixel clustering and of the energy dependence of the signal can be appreciated more clearly from Fig. 5 in which phase contrast and CNR are calculated for each bin. In the low-energy part of the spectrum (4-20 keV), clustering methods increase phase contrast by suppressing the strong, spurious low-energy peak due to the charge sharing counts. The CNR results show that most of the CNR contribution is located near the tungsten emission lines due to both greater contrast and to the higher number of counts. An improvement in the statistics of the high-energy events is also noticed, which leads to higher CNR above 20 keV. This improvement would be beneficial in the imaging of materials with higher atomic number, for which the highest contribution to contrast and CNR may not arise from the low-energy part of the spectrum.
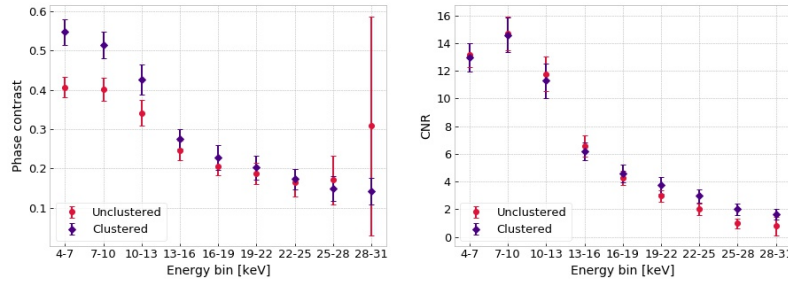

Fig. 5. Contrast (left) and CNR (right) as a function of the energy bin for the 30 kVp image with FSP XPCI.

3.3.   Image comparison and energy-weighting

Finally, Fig. 6 compares unclustered and the energy-weighted images for FSP XPCI at 50 kVp and SM-EI XPCI at 30 kVp. The full unclustered images correspond to the unweighted sum of all energy channels without clustering (the ones in Fig. 4a for FSP at 30 kVp), whereas the energy-weighted images are the weighted sum of all energy channels with clustering (Fig. 4b for FSP at 30kVp), using the weighting factors presented in eq. 3. The increase in attenuation contrast due to clustering and energy weighting is apparent, as it is the increased edge enhancement due to phase effects which is more clearly noticeable in the horizontal profiles reported below each corresponding image. These allow observing that the contrast is significantly higher in SM-EI XPCI than in FSP XPCI (64% when comparing the energy- weighted images at 30 kVp), despite the significantly reduced magnification employed. However, this does not translate directly into a CNR increase due to reduced statistics per pixel and additional image noise caused by mask vibrations and/or focal spot instabilities. With regards to statistics, since the use of dithering in the SM-EI XPCI acquisitions produced an image with 4 times higher resolution than in the FSP case, and the overall exposure has been kept the same for the full image, the statistics per pixel are substantially reduced by a factor of 4 in the SM-EI case, which should be multiplied by the factor of approximately 8 due to the limited open fraction of the mask. With respect to set-up instabilities, system geometry variations over time due to vibrations or temperature fluctuations have been previously studied for other edge illumination configurations, and their influence on the set-up sensitivity was demonstrated [46]. We expect these effects to be relevant to our set-up because the low power microfocus X-ray source imposes relatively long exposure times, which increases the possible impact of such environmental changes. Although a detailed analysis of the effects of such time-dependent variations would become key for a possible commercial translation of the developed technique, at present time we considered it to lie beyond the scope of this initial explorative work.
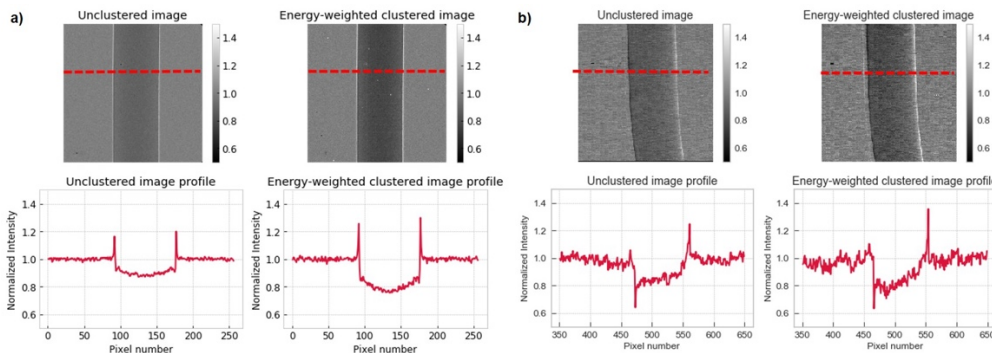

Fig. 6. Image comparison between the unclustered image and the energy-weighted image with clustering for FSP XPCI at 50 kVp (a) and SM-EI XPCI at 30 kVp (b). The averaged horizontal profiles along the five indicated rows are also shown for each of the measurements (c)-(d).

07 Contrast and CNR calculations for the three experimental measurements are presented in Tables 1 and 2. In all cases,
08 it is found that greater levels of contrast and CNR can be achieved by using spectral methods. This is first observed
09 with pixel clustering, and further improved by energy-weighting. When comparing the energy-weighted images with the
10 unclustered images, contrast is increased by 36%, 70% and 53% for the FSP XPCI at 30 kVp, FSP XPCI at 50 kVp
11 and SM-EI XPCI at 30 kVp measurements, respectively.

12

13 Likewise, CNR is increased by 7%, 19% and 12% with energy-weighting and pixel clustering with respect to the
14 unclustered images, for the same three measurements. The smaller changes on the CNR are due to compensation
15 between higher contrast and reduced statistics due to clustering, seen as an increment in noise. Finally, note that X-
16 ray energy being equal, clustering leads to a larger relative improvement for the SM-EI XPCI technique, due to the high
17 sensitivity of its working principle to charge sharing. Pixel clustering in SM-EI generates larger error bars for both
18 clustered images, since photons impinging close to a pixel edge can be erroneously allocated to the adjacent pixel,
19 leading to variations in the position of the maximum peak of the phase signal.

20

	Full image (unclustered)	*Full image (clustered)*	*Energy-weighted (clustered)*
FSP XPCI 30 kVp	0.33 ± 0.03	0.35 ± 0.03	0.42 ± 0.03
FSP XPCI 50 kVp	0.27 ± 0.03	0.32 ± 0.03	0.41 ± 0.05
SM-EI XPCI 30 kVp	0.45 ± 0.05	0.65 ± 0.10	0.69 ± 0.11

Table 1. Contrast results for unclustered images, clustered images without weighting and energy weighted images for the three experimental measurements.

21

	Full image (unclustered)	*Full image (clustered)*	*Energy-weighted (clustered)*
FSP XPCI 30 kVp	23 ± 2	23 ± 2	25 ± 2
FSP XPCI 50 kVp	18 ± 2	19 ± 2	22 ± 2
SM-EI XPCI 30 kVp	11 ± 1	12 ± 2	12 ± 2

Table 2. CNR results for unclustered images, clustered images without energy weighting and energy-weighted images for the three experimental measurements.

22
23
24 4. **Summary**

25

26 The present work demonstrates that the spectroscopic capabilities of the Timepix3 detector can improve image quality
27 in the two XPCI techniques studied. Also, that the small pixel pitch of the Timepix3 favors the FSP XPCI principle and
28 that the sharp pixel PSF of the detector allows the implementation of SM-EI XPCI. The effect of pixel clustering and
29 energy weighting in phase contrast and CNR was quantified for both the FSP and SM-EI XPCI techniques. The
30 relevance of clustering methods to exploit the information carried by all photons and the energy dependence of phase
31 contrast and CNR in XPCI was studied.
32 In all cases, an enhancement of image quality with respect to single-threshold photon-counting detectors was
33 observed; this allows to assume that, in comparison, any non-counting detector would be penalized at least to the
34 same extent as a single threshold counter, if not worse. A higher improvement in phase contrast is obtained for FSP
35 XPCI at 50 kVp as compared to 30 kVp, because spectral corrections become more relevant at higher X-ray energies
36 due to charge sharing. A significant contrast enhancement is achieved (over 20% for both voltage settings: 30 kVp and
37 50 kVp) for FSP XPCI with a weighted average over all nine energy windows considered (4-7 keV through 28-31 keV
38 for the 30 kV case), with the calculated phase contrast as weighting factor. The SM-EI XPCI technique shows a much
39 higher contrast than FSP XPCI, and the difference in contrast between the two methods gets further enhanced by pixel
40 clustering and energy-weighting. These results confirm that the coupling of phase-sensitive methods with single photon

energy measurement technologies could boost the potential of X-ray phase contrast imaging for a wide variety of applications.

Acknowledgement

References

[1] M. Endrizzi, X-ray phase contrast imaging, Nucl. Instrum. Methods Phys. Res. A, 878 (2018) 88–98.

[2] A. Bravin, P. Coan, P. Suortti, X-ray phase contrast imaging: from pre-clinical applications towards clinics, Phys. Med. Biol., 58 (1) (2012) R1–R35.

[3] P. Russo, Handbook of X-ray Imaging: Physics and Technology, 1st ed., CRC Press, Boca Raton, 2017.

[4] S.-A. Zhou, A. Brahme, Development of phase-contrast X-ray imaging techniques and potential medical applications, Phys. Med., 24 (3) (2008) 129–148.

[5] P. Coan, A. Bravin, G. Tromba, Phase-contrast X-ray imaging of the breast: recent developments towards clinics, J. Phys. D: Appl. Phys., 46 (49) (2013) 494007.

[6] A. Stevenson, T. Gureyev, D. Paganin, S. Wilkins, T. Weitkamp, A. Snigirev, C. Rau, I. Snigireva, H. Youn, I. Dolbnya, W. Yun, B. Lai, R. F. Garrett, D. J. Cookson, K. Hyodo, M. Ando, Phase-contrast X-ray imaging with synchrotron radiation for materials science applications, Nucl. Instrum. Methods Phys. Res. B, 199 (2003) 427–435.

[7] S.C. Mayo, A.W. Stevenson, S.W. Wilkins, In-line phase-contrast X-ray imaging and tomography for materials science, Materials, 5 (5) (2012) 937–965.

[8] E. A. Miller, T. A. White, B. S. McDonald, A. Seifert, Phase Contrast X-Ray Imaging Signatures for Security Applications, IEEE Transactions on Nuclear Science, 60 (1) (2013) 416-422.

[9] M. Uehara, W. Yashiro, A. Momose, Effectiveness of X-ray grating interferometry for non-destructive inspection of packaged devices, J. Appl. Phys., 114 (2013) 134901.

[10] H. Einarsdóttir, M. J. Emerson, L. H. Clemmensen, K. Scherer, K. Willer, M. Bech, R. Larsen, B. K. Ersbøll, F. Pfeiffer, Novelty detection of foreign objects in food using multi-modal X-ray imaging, Food Control, 67 (2016) 39-47.

[11] A. Snigirev, I. Snigireva, V. Kohn, S. Kuznetsov, I. Schelokov, On energy synchrotron radiation, Rev. Sci. Instrum., 66 (12) (1995) 5486-5492.

[12] S. W. Wilkins, T. E. Gureyev, D. Gao, A. Pogany, A. W. Stevenson, Phase-contrast imaging using polychromatic hard X-rays, Nature, 384 (1996) 335–338.

[13] P. Cloetens, M. Pateyron-Salome, J. Y. Buffiere, G. Peix, J. Baruchel, F. Peyrin, M. Schlenker, Observation of microstructure and damage in materials by phase sensitive radiography and tomography, J. Appl. Phys., 81 (1997) 5878–5886.

[14] S. W. Wilkins, D. Gao, T. Gureyev, A. Pogany, A. W. Stevenson, X-ray phase-contrast radiography, Radiology, 205 (1997) 907–907.

[15] O. Betz, U. Wegst, D. Weide, M. Heethoff, L. Helfen, W. Lee, P. Cloetens, Imaging applications of synchrotron X-ray phase-contrast microtomography in biological morphology and biomaterials science. I. General aspects of the technique and its advantages in the analysis of millimetre-sized arthropod structure, J. Microscopy, 227 (2007) 51-71.

[16] Y. Liu, J. Nelson, C. Holzner, J. C. Andrews, P. Pianetta, Recent advances in synchrotron-based hard x-ray phase contrast imaging, J. Phys. D: Appl. Phys., 46 (49) (2013) 494001.

[17] B. Zoofan, J. Y. Kim, S. I. Rokhlin, G. S. Frankel, Phase-contrast x-ray imaging for nondestructive evaluation of materials, J. Appl. Phys., 100 (2006) 014502.

[18] T. Zhou, U. Lundström, T. Thüring, S. Rutishauser, D. H. Larsson, M. Stampanoni, C. David, H. M. Hertz, A. Burvall, Comparison of two x-ray phase-contrast imaging methods with a microfocus source, Opt. Express, 21 (25) (2013) 30183-30195.

[19] M. A. Beltran, D. M. Paganin, K. Uesugi, M. J. Kitchen, 2D and 3D X-ray phase retrieval of multi-material objects using a single defocus distance, Opt. Express, 18 (7) (2010) 6423-6436.

[20] T. Weitkamp, D. Haas, D. Wegrzynek, A. Rack, ANKAphase: software for single-distance phase retrieval from inline X-ray phase-contrast radiographs, J. Synchrotron Radiat., 18 (4) (2011) 617-629.

[21] R. C. Chen, H. L. Xie, L. Rigon, R. Longo, E. Castelli, T. Q. Xiao, Phase retrieval in quantitative x-ray microtomography with a single sample-to-detector distance, Opt. Lett., 36 (9) (2011) 1719-1721.

[22] K. Nugent. K. A. Nugent, X-ray noninterferometric phase imaging: a unified picture, J. Opt. Soc. Am. A, 24 (2007) 536–546.

[23] A. Olivo, F. Arfelli, G. Cantatore, R. Longo, R. H. Menk, S. Pani, M. Prest, P. Poropat, L. Rigon, G. Tromba, E. Vallazza, E. Castelli, An innovative digital imaging set-up allowing a low-dose approach to phase contrast applications in the medical field, Med. Phys., 28 (8) (2001) 1610–1619.

[24] A. Olivo, R. Speller. A coded-aperture technique allowing X-ray phase contrast imaging with conventional sources. Appl. Phys. Lett., 91 (2007) 074106.

[25] F. Krejci, J. Jakubek, M. Kroupa, Hard x-ray phase contrast imaging using single absorption grating and hybrid semiconductor pixel detector, Rev. Sci. Instrum., 81 (11) (2010) 113702.

[26] G. K. Kallon, P. C. Diemoz, F. A. Vittoria, D. Basta, M. Endrizzi, A. Olivo, Comparing signal intensity and refraction sensitivity of double and single mask edge illumination lab-based x-ray phase contrast imaging set-ups, J. Phys. D: Appl. Phys., 50 (41) (2017) 415401.

[27] F. Krejci, J. Jakubek, M. Kroupa, Single grating method for low dose 1D and 2D phase contrast x-ray imaging, J. Instrum., 6 (2011) C01073.

[28] J. Zemlicka, J. Dudak, D. Kubanda, F. Krejci, Single absorption grating based X-ray phase contrast CT using Timepix detector, J. Instrum., 14 (2019) C05007.

[29] D. Gürsoy, M. Das, Single-step absorption and phase retrieval with polychromatic x rays using a spectral detector. Opt. Lett., 38 (9) (2013) 1461-1463.

[30] M. Das, Z. Liang, Spectral x-ray phase contrast imaging for single-shot retrieval of absorption, phase, and differential-phase imagery. Opt. Lett., 39 (21) (2014) 6343-6346.

[31] Z. Wang, K. Gao, D. Wang, Z. Wu, H. Chen, S. Wang, Z. Wu, Single-shot x-ray phase imaging with grating interferometry and photon-counting detectors, Opt. Lett., 39 (4) (2014) 877-879.

[32] J. Giersch, D. Niederlöhner, G. Anton, The influence of energy weighting on X-ray imaging quality. Nucl. Instrum. Meth. Phys. Res. A, 531 (2004) 68–74.

[33] L. Karg, D. Niederlöhner, J. Giersch, G. Anton, Using the Medipix2 detector for energy weighting. Nucl. Instrum. Meth. Phys. Res. A, 546 (2005) 306–311.

[34] G. Pelzer, T. Weber, G. Anton, R. Ballabriga, F. Bayer, M. Campbell, W. Haas, F. Horn, X. Llopart, N. Michel, U. Mollenbauer, J. Rieger, A. Ritter, I. Ritter, S. Woelfel, W. S. Wong, A. Zang, T. Michel, Energy weighting in grating-based X-ray phase-contrast imaging, in SPIE Med. Imag. 2014: Phy. Med. Imag., San Diego, CA, United States, 2014, 903352.

[35] M. Endrizzi, F. Vittoria, G. Kallon, D. Basta, P. Diemoz, A. Vincenzi, P. Delogu, R. Bellazzini, A. Olivo, Achromatic approach to phase-based multi-modal imaging with conventional X-ray sources, Opt. Express, 23 (12) (2015) 16473.

[36] T. Poikela, J. Plosila, T. Westerlund, M. Campbell, M. D. Gaspari, X. Llopart, V. Gromov, R. Kluit, M. V. Beuzekom, F. Zappon, V. Zivkovic, C. Brezina, K. Desch, Y. Fu, A. Kruth, Timepix3: a 65K channel hybrid pixel readout chip with simultaneous ToA/ToT and sparse readout, J. Instrum., 9 (5) (2014) C05013.

[37] T. Billoud, C. Leroy, C. Papadatos, M. Pichotka, S. Pospisil, J. Roux, Characterization of a pixelated CdTe Timepix detector operated in ToT mode, J. Instrum., 12 (1) (2017) P01018.

[38] S. Procz, C. Avila, J. Fey, G. Roque, M. Schuetz, E. Hamann, X-ray and gamma imaging with Medipix and Timepix detectors in medical research, Radiat. Meas., 127 (2019) 106104.

[39] D. Turecek, J. Jakubek, E. Trojanova, L. Sefc, V. Kolarova, Application of Timepix3 based CdTe spectral sensitive photon counting detector for PET imaging, Nucl. Instrum. Meth. Phys. Res. A, 895 (2018) 84-89.

[40] C. Granja, S. Polansky, Z. Vykydal, S. Pospisil, A. Owens, Z. Kozacek, K. Mellab, M. Simcak, The SATRAM Timepix spacecraft payload in open space on board the Proba-V satellite for wide range radiation monitoring in LEO orbit, Planet. Space Sci., 125 (2016) 114-129.

[41] D. Turecek, J. Jakubek, E. Trojanova, L. Sefc, Compton camera based on Timepix3 technology, J. Instrum., 13, (2018) C11022.

[42] P. Diemoz, F. Vittoria, A. Olivo, Spatial resolution of edge illumination X-ray phase-contrast imaging, Optics Express, 22 (13) (2014) 15514.

[43] J. Jakubek, Precise energy calibration of pixel detector working in time-over-threshold mode, Nucl. Instrum. Meth. Phys. Res. A, 633 (2004) 262-266.

[44] J. Jakubek, Energy-sensitive X-ray radiography and charge sharing effect in pixelated detector, Nucl. Instrum. Meth. Phys. Res. A, 607 (2009) 192-195.

[45] T. G. Schmidt, Optimal "image-based" weighting for energy-resolved CT, Med. Phys., 36 (2009) 3018-3027.

[46] A. Zamir, M. Endrizzi, C. Hagen, F. Vittoria, L. Urbani, P. De Coppi, A. Olivo, Robust phase retrieval for high resolution edge illumination x-ray phase-contrast computed tomography in non-ideal environments, Sci Rep, 6 (2016) 31197.